



Assessment of Changes of Complex Shoreline from Medium-Resolution Satellite Imagery

Nikolay P. Nezlin^{1,2} · Julie D. Herman³ · Jonathan Hodge⁴ · Stephen Sagar⁵ · Robbi Bishop-Taylor⁵ · Guangming Zheng^{1,6} · Paul M. DiGiacomo¹

Received: 21 February 2023 / Revised: 3 August 2023 / Accepted: 4 August 2023 / Published online: 19 August 2023
© The Author(s), under exclusive licence to Coastal and Estuarine Research Federation 2023

Abstract

The imagery collected by medium-resolution earth-observing satellites is a powerful and cost-effective tool for the quantitative assessment of shoreline dynamics for water bodies of different spatial scales. In this study, we utilize imagery collected in 1984–2021 on the Middle Peninsula, Virginia, bordering the Chesapeake Bay, USA, by medium-resolution (10–30 m) satellites Landsat-5/7/8 and Sentinel-2A/B. The data was managed in the Earth Analytics Interoperability Lab (EAIL) Data Cube built and configured by the Commonwealth Scientific and Industrial Research Organization (CSIRO, Australia and Chile). The assessments of shoreline change demonstrate adequate agreement with assessments based on aerial photography collected during 1937–2009 by the Virginia Institute of Marine Science, with reasonable disagreement attributed to the differences in the analyzed periods and in the accuracy of land/water edge detection. Most of the studied coastline was subject to land loss (erosion), in some locations exceeding 3 m year⁻¹, usually along low-lying sandy beaches. The shoreline segments with man-made structures such as marinas, bulkheads, revetments, and offshore breakwaters demonstrated a significantly lower range of changes as compared to natural reaches. Regular analysis of medium-resolution satellite imagery appears to be an effective method for routine assessment of shoreline changes along the land/water edge.

Keywords Coast · Shoreline change · Satellite imagery · Chesapeake Bay

Introduction

The land zones located along ocean coasts include most populated and developed areas in the world (Small & Nicholls 2003). Reliable assessments of how a particular coast has

Communicated by Brian B. Barnes

✉ Nikolay P. Nezlin
nikolay.nezlin@noaa.gov

¹ NOAA/NESDIS Center for Satellite Applications and Research, College Park, MD, USA

² Global Science & Technology, Inc, Greenbelt, MD, USA

³ Virginia Institute of Marine Science, Gloucester Point, VA, USA

⁴ Commonwealth Scientific and Industrial Research Organization (CSIRO) Chile, Región Metropolitana, Santiago, Chile

⁵ Digital Earth Branch, Geoscience Australia ACT, Canberra, Australia

⁶ Cooperative Institute for Satellite Earth System Studies, Earth System Science Interdisciplinary Center, University of Maryland, College Park, MD, USA

changed through time and how it might proceed in the future are therefore important challenges directly related to ecosystem vulnerability, human safety, and economic development (Neumann et al. 2015; Mills et al. 2021; O'Hara & Halpern 2022) and, as such, are a focus of intensive research worldwide (Parthasarathy & Deka 2021; Rahman et al. 2022).

Substantial changes in the shoreline are observed over most of the Earth's surface (Pekel et al. 2016; Mentaschi et al. 2018; Murray et al. 2022). These changes are predominantly associated with natural processes like winds, waves, tides, and currents, which modify coastlines by eroding, transporting, and depositing sediments (Mentaschi et al. 2018). Changes in relative sea level are one of two primary long-term processes which cause the shoreline to move; the other is wave action, particularly during storms. Although shoreline change is mostly a natural process, human activity through shoreline hardening or inlet stabilization also plays a crucial role, affecting the resistance/resilience of the coastline (Armstrong & Lazarus 2019; Mendoza et al. 2022).

Traditional assessment methods of rates of shoreline change utilize the data collected in land-based surveys or imagery from aerial platforms (photographs or lidar),

which is a laborious and expensive task (Luijendijk et al. 2018; Apostolopoulos & Nikolakopoulos 2021; Castelle et al. 2021). In recent decades, the increasing volumes of high- and medium-resolution satellite observations have provided a powerful alternative to obtain reliable shoreline data (Splinter et al. 2018; Vos et al. 2019a; Apostolopoulos & Nikolakopoulos 2021). For any chosen region globally, the Landsat series of satellites provides data approximately every 2 weeks, resulting in hundreds of available images over several decades. More recently, the ease of use of satellite imagery has dramatically improved, including from the use of data cube technology, allowing users to operate big Earth observations (EO) data at a minimum cost and effort (Lewis et al. 2017; Giuliani et al. 2019; Sudmanns et al. 2022).

Most studies using high- and medium-resolution satellite imagery for the analysis of shoreline change are focused on

small areas at specific locations, mostly sandy beaches, and use algorithms of shoreline change detection based on cross-shore transects (Himmelstoss et al. 2018; Vos et al. 2019a, 2020; Bishop-Taylor et al. 2021). This approach works well in regions with straight coastlines, but often results in erroneous assessments in areas with complex (indented, embayed) shorelines, where applying baseline transects orthogonal to the coast is problematic in both convex and concave parts of the shoreline (Mentaschi et al. 2018). The area of this study, the Middle Peninsula located in coastal Virginia by the Chesapeake Bay (Fig. 1), is characterized by complex shorelines and, as such, requires an improved approach for detection of shoreline changes.

For assessments of the rates of shoreline change using satellite imagery, we did not focus on accurate detection of the instantaneous land/water interface at different time periods. The term “shoreline” implies a range of indicators

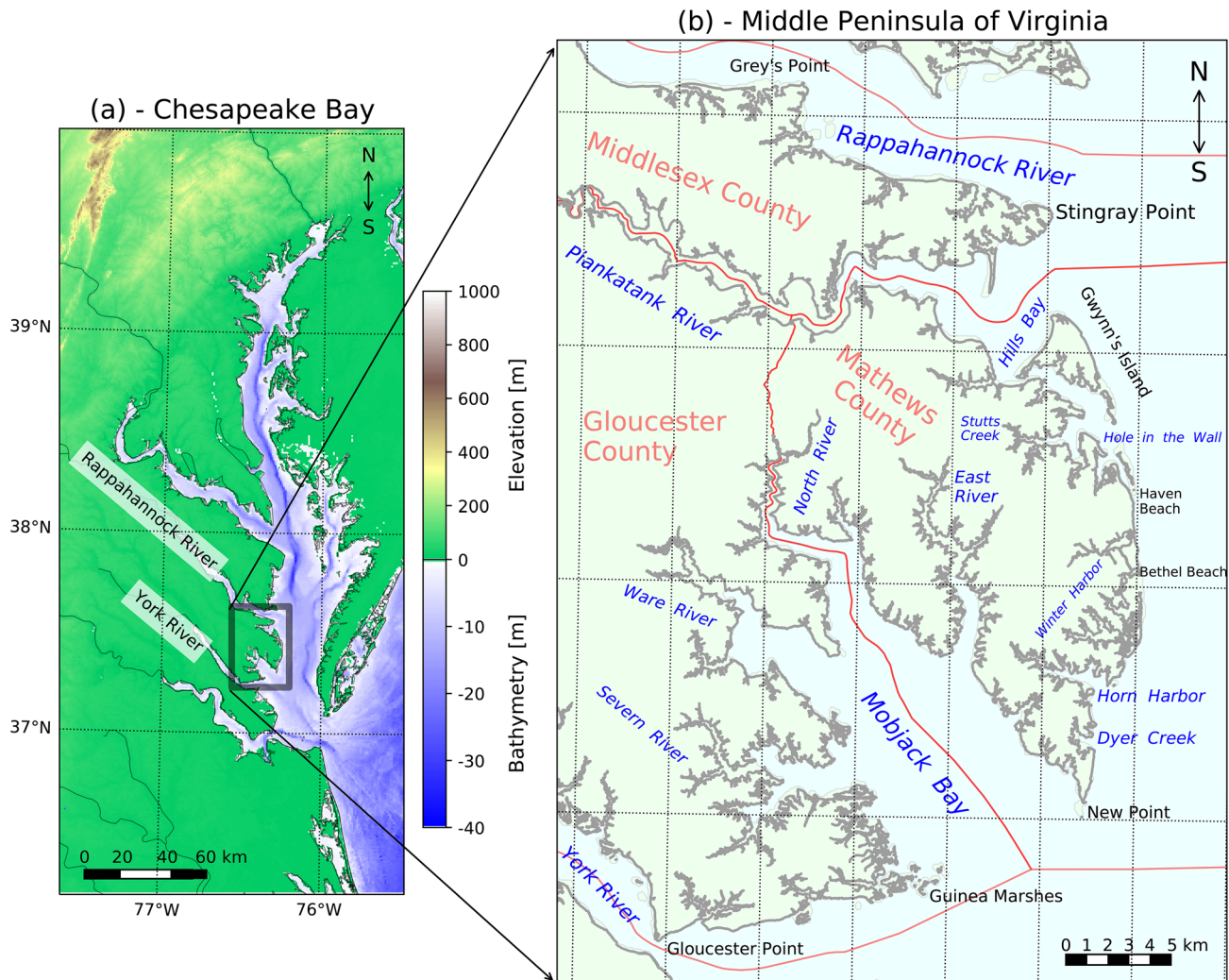


Fig. 1 **a** Location of the Middle Peninsula of Virginia within the Chesapeake Bay estuarine system; **b** eastern part of Middle Peninsula where shoreline change was analyzed. The boundaries and names of counties are in red

associated with the boundaries visible at satellite images, including seaward vegetation edge, wet/dry line, instantaneous water line, and surf zone, and the horizontal offset between these features can be of the order of several tens of meters (Thieler & Danforth 1994; Boak & Turner 2005). However, all these indicators are directed alongshore, and their displacement associated with erosion/accretion is expected to proceed onshore/offshore and with comparable rates (Almonacid-Caballer et al. 2016). Therefore, we assumed that the obtained rates of shoreline change are acceptable regardless of which shoreline indicator dominated in the satellite imagery analyzed in this study.

Here, we focus on (1) developing a remote-sensing method for assessing coastal change that is suitable for both straight and complex shorelines; (2) applying this method to satellite imagery collected over the Middle Peninsula; (3) comparing the obtained rates of shoreline change (erosion/accretion) to data from aerial photography considering the potential sources of disagreement; and (4) analyzing the effect of coastal morphology, land cover, and man-made shoreline structures on the rates of shoreline change. The structure of the paper is arranged as follows: the second section describes the study area; the third section details the satellite and aerial photography data used for assessments of shoreline displacement; and the fourth section presents the results of the study. A discussion of the results is then presented in the fifth section, followed by the conclusions of the study in the sixth section.

The Study Area: Middle Peninsula, Virginia, by the Chesapeake Bay

The Middle Peninsula is located on the western shore of the lower Chesapeake Bay in Virginia, along the East Coast of the USA (Fig. 1a). This region is bounded by the Rappahannock River on the north and the York River on the south, both estuarine tributaries that flow southeast into the Chesapeake Bay. The Middle Peninsula is a part of the Virginia Coastal Plain and has a relatively low-lying topography (Fig. 1a), although there are reaches along the rivers with higher bluffs. The Middle Peninsula's lower part includes three Virginia counties: Gloucester, Mathews, and Middlesex. With a population of just over 90,000 and a 10-year growth rate of 9% (<https://www.mpava.com/regional-profile>), the Middle Peninsula is a rural area with no cities and little industry. Major sources of income are farming, fishing, aquaculture, tourism, business services, and recreational activities. The Middle Peninsula coastline includes thousands of acres of ecologically valuable tidal and non-tidal wetlands, forests, agricultural lands, rivers, streams, and beaches that play important roles in the lives of the local population. However, increasing population pressure as more people move to coastal areas means more changes

along shorelines as property owners install living shorelines (preferred shoreline protection strategy) or riprap (hardened structures to prevent erosion in high energy environments).

The rate of relative sea level rise (RSLR) on the Middle Peninsula area (an average of 4.93 mm year⁻¹ during 1950–2021, measured in Yorktown, VA; <https://tidesandcurrents.noaa.gov/slrends/slrends.html>) significantly exceeds the global mean sea level rise estimated as 1.7 to 3.2 mm year⁻¹, depending on the time period examined (Cazenave & Llovel 2010; Church & White 2011). One reason is that the land in this area is subsiding due to groundwater withdrawal estimated as 1.5 to 3.7 mm year⁻¹ in different parts of Virginia (Pope & Burbey 2004). As a result, the Middle Peninsula area is more vulnerable to RSLR than many other coastal regions, causing receding shorelines and erosion of the bank material providing sediments for wetlands, offshore bars, beaches, and dunes, but also affecting the bay's water quality.

Compared with other estuaries, tidal forcing in the Chesapeake Bay is modest with the tidal range rarely exceeding 1 m (Zhong & Li 2006; Zhong et al. 2008) and an average tide range in the Virginia portion of the Chesapeake Bay about 0.6 m (<https://tidesandcurrents.noaa.gov/map/index.html?type=datums®ion=Virginia>). Wind-driven waves are a major source of erosion. They erode and redistribute sediment as well as undercut higher bluffs, which causes slumping and bank retreat. The height of waves is dependent partly on water depth and fetch. Fetch is the distance across the water surface that the wind blows. Longer fetches usually result in higher waves. On the Middle Peninsula, the wind directions can vary but two major types of storms produce the largest waves; they are nor'easters (which bring winds from the northeast) and hurricanes (which have varying tracks and therefore wind directions but tend to come from the south and move in a mostly northerly direction). The side of the river (north shore or south shore) can affect erosion rates (Hardaway & Byrne 1999), with south shores (i.e., north-facing) tending to have higher rates than north shores (south facing), and creeks and sheltered embayments having much lower rates.

Data and Methods

Satellite Data

The satellite data used for assessment of satellite-derived shoreline (SDS) displacement were collected between 1984 and 2021 (38 years) by medium-resolution Earth-observing (EO) satellites Landsat-5/7/8 and Sentinel-2A/B (Fig. 2). The level 2 (atmospherically corrected surface reflectance) data files obtained from the Amazon Web Services (AWS) were managed in the Earth Analytics Interoperability Lab (EAIL) Data Cube built and configured by the

Commonwealth Scientific and Industrial Research Organization (CSIRO, Australia and Chile) and hosted on AWS with the support of the Chilean Data Observatory (www.dataobservatory.net). The EAIL Data Cube is based on the paradigm of EO data cubes (EODCs), which are an approach for the management and analytics of multi-dimensional EO data and can be operated on a variety of scales and infrastructures. EODC implementations enhance connections between data, applications, and users facilitating management, access, and use of analysis ready, cloud-optimized data (ARCO), providing instruments for efficient data discovery, view, access, and processing (Lewis et al. 2017; Giuliani et al. 2019; Sudmanns et al. 2022). EAIL is a robust cloud-based platform based on Open Data Cube (ODC – www.opendatacube.org) and makes use of modern cloud technologies for its underlying architecture and to deliver scalable analytics capabilities, automated data processing, and ingestion workflows.

This study utilized imagery collected by the Landsat (Loveland & Dwyer 2012) and Copernicus' Sentinel (Aschbacher & Milagro-Pérez 2012) missions. The Landsat program, jointly operated by the National Aeronautics and Space Administration (NASA) and the US Geological Survey (USGS), collects space-based imagery at moderate (30 m) spatial resolution. In this study, we use the images acquired by the Thematic Mapper (TM) on-board Landsat 5 (1984–2011), the Enhanced Thematic Mapper Plus (ETM+) on-board Landsat 7 (1999–present), and the Operational Land Imager (OLI) on-board Landsat 8 (2013–present) (Fig. 2). The revisit time of each Landsat satellite is 16 days. The Scan Line Corrector (SLC) of Landsat 7 ETM+ has failed since 31 May 2003, causing the scanning pattern to exhibit wedge-shaped scan-to-scan gaps, leading to images that are missing approximately 22% of the normal scene area (Maxwell et al. 2007; Lee et al. 2016; Li et al. 2017).

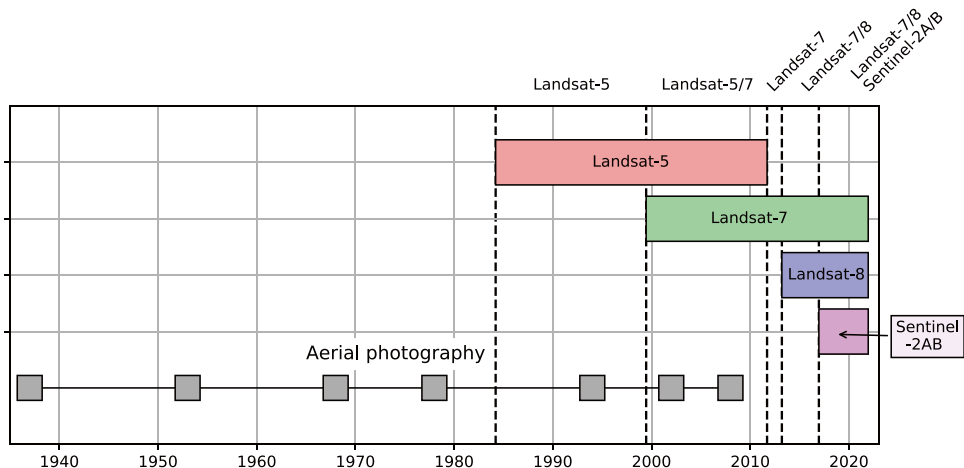
Fig. 2 The periods of aerial photography and satellite observations (Landsat-5/7/8 and Sentinel-2A/B). Sentinel-2A and Sentinel-2B were launched on June 23, 2015, and March 7, 2017, but in the Earth Analytics Interoperability Lab (EAIL) Data Cube the data collected by both Sentinel-2 satellites are represented as one product starting January 2017. Dashed vertical lines indicate the periods when the number of observing satellites changed

The twin satellites, Sentinel-2A and 2B with Multi-Spectral Instruments (MSI) onboard, are the part of the European Union's Copernicus program. Sentinel-2A and Sentinel-2B were launched on June 23, 2015, and March 7, 2017, but in the EAIL Data Cube, the data collected by both Sentinel-2 satellites is represented as one product starting January 2017. The Sentinel-2 satellites provide both higher spatial, temporal (5 days), and spectral resolution optical data compared to Landsat (Drusch et al. 2012). The spatial resolution of optical bands used in this study is 10 m ("green" band 3) and 20 m ("red edge" band 6), both transformed to 30 m resolution in EAIL.

We call the resulting imagery (30 m) resolution "medium", following the terminology (mid-, moderate-, medium-) used by many Landsat and Sentinel-2 explorers (Pardo-Pascual et al. 2018; Bishop-Taylor et al. 2019, 2021; McAllister et al. 2022), which use the term "high resolution" for aerial photography and/or satellite imagery of < 5 m pixel size (WorldView-2, Planet Labs Inc. SkySat satellites, etc.). At the same time, many researchers call Landsat and Sentinel-2 spatial resolution "high" (Drusch et al. 2012; Liu et al. 2012; Zhu & Woodcock 2012; Verpoorter et al. 2014), usually comparing it to Moderate Resolution Imaging Spectroradiometer (MODIS), with a spatial resolution of 250–1000 m. On the other hand, Apostolopoulos and Nikolakopoulos (2021) in their review classify Landsat as low-resolution (> 20 m) and Sentinel-2 as medium-resolution data for coastline change monitoring.

The temporal density of satellite observations varied during different periods of the study, affecting the statistical power of the results. Specifically, the periods before June 1999 and between September 2011–March 2013 included observations of only one satellite (Landsat-5 and Landsat-7, respectively) (Fig. 2) and, as such, should be treated with caution.

Images were extracted and processed separately for each of the four satellite products stored in the EAIL Data Cube (Landsat-5, Landsat-7, Landsat-8 and Sentinel-2A/B).



Regardless of the spatial resolution of satellite sensors (30 m for Landsat-5/7/8 and 10–20 m for Sentinel-2A/B), all analysis-ready images were extracted from the data cube in a consistent spatial resolution (30 m) for 105 rectangular regions of 1–5 km size along the Middle Peninsula shoreline (Fig. 3a). By resampling and decreasing the spatial resolution of Sentinel-2, we assume that this parameter does not play a significant role in SDS detection accuracy (Hagenaars et al. 2018; Vos et al. 2019a).

Taking into account that tidal stage is one of the most important factors influencing short-term fluctuations in SDS position (Bishop-Taylor et al. 2021; Nanson et al. 2022), we analyzed only the images collected during intermediate (25–75%) tide levels, excluding 25% of the images collected during high and 25% collected during low tides. The tidal model FES2014 (Lyard et al. 2021) was used to calculate the tide heights at the exact time of each satellite image acquisition for the points closest to the center of each analyzed region and at least 1 km offshore. The images were classified into three groups: 25% collected during high tide; 50% collected during mid-tide; and 25% collected during low tide. The high-tide and low-tide groups were excluded from

analysis. We do not expect the remaining small tidal variations of the water levels to affect SDS significantly because this effect occurs in the areas with shallow shore face slopes (beaches), where specific methods of tidal correction are applied (Vos et al. 2019a, b, 2020; Bishop-Taylor et al. 2021). In the study area, only 6% of the shoreline (269 of 4530 analyzes locations) were classified as “beaches”, with other areas having higher slopes.

In satellite images, pixels of suspicious quality were eliminated, i.e., replaced with “no data” code. For Landsat-5/7/8, the pixels with quality codes “high cloud confidence” and “high cloud shadow confidence” were eliminated. For Sentinel-2A/B, the pixels with quality codes “cloud high probability”, “cloud medium probability”, “thin cirrus”, “cloud shadows”, and “saturated or defective” were eliminated. After that, the images with less than 50% of “good” pixels were excluded from the analysis.

All “good” pixels were classified as “land” or “water” using the Modified Normalized Difference Water Index (MNDWI) (Xu 2006), also called Land Surface Water Index (LSWI) (Xiao et al. 2002; Bera & Maiti 2019). MNDWI was calculated from the surface reflectances using the equation $MNDWI = (Green - Red) / (Green + Red)$

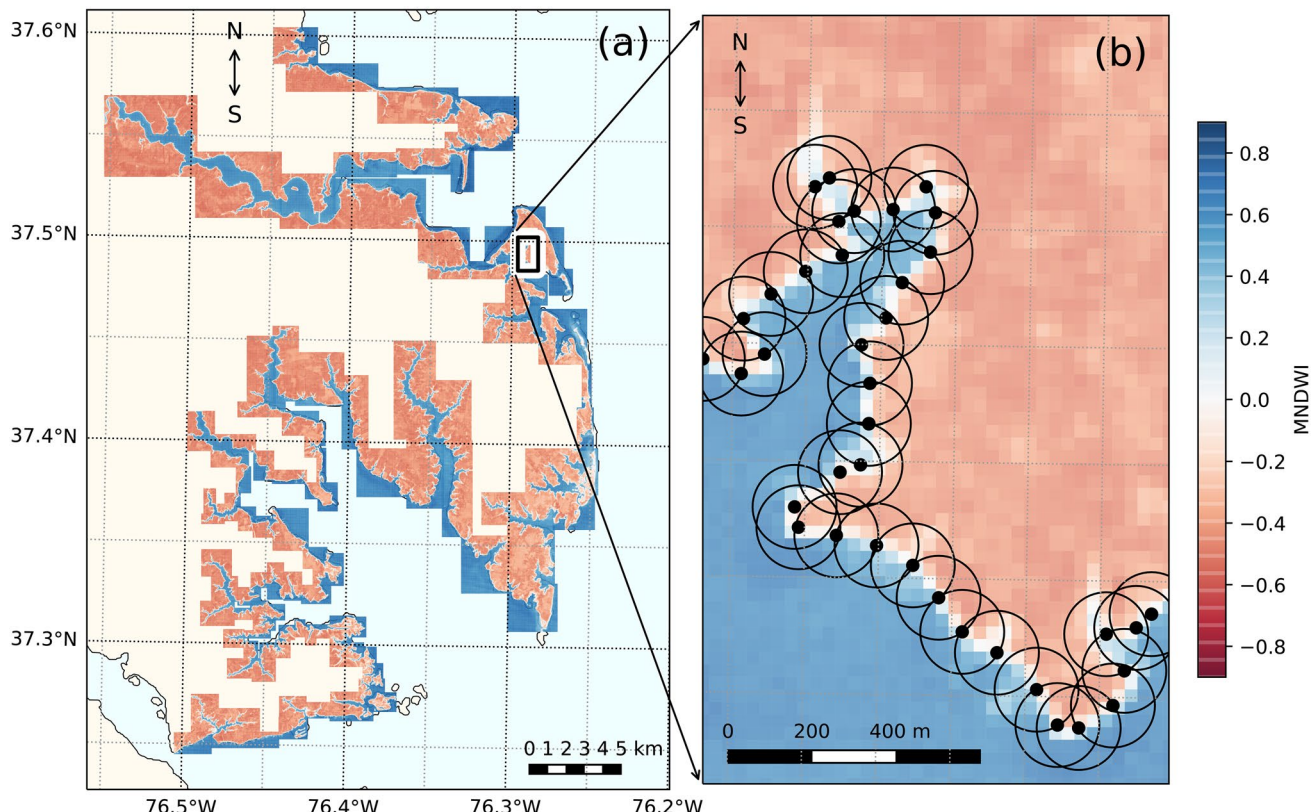


Fig. 3 **a** Rectangular regions with satellite data extracted from EAIL Data Cube; **b** one region with 100-m circles along the shoreline where the rates of coastal change (“land loss/erosion” vs. “land gain/accretion”) were calculated. The color in **b** is Modified Normalized

Difference Water Index (MNDWI) averaged from four Earth Analytics Interoperability Lab (EAIL) Data Cube satellite products (Landsat-5, Landsat-7, Landsat-8, and Sentinel-2A/B). In MNDWI, deeper blue/red indicates higher confidence that it's water/land

$- SWIR) / (Green + SWIR)$, where *Green* is the surface reflectance at green band (band 2 for Landsat-5/7 and band 3 for Landsat-8 and Sentinel-2A/B) and *SWIR* is the surface reflectance at shortwave infrared band (band 5 for Landsat-5/7 and band 6 for Landsat-8 and Sentinel-2A/B). High MNDWI values indicate water, low values indicate a non-water or land surface, and maximum MNDWI gradient between them indicates shoreline (Fig. 3b). Numerous indices increasing the contrast between water and land pixels in the image have been developed and used for shoreline detection, including Normalized Difference Water Index (NDWI), Water Index, Normalized Difference Vegetation Index (NDVI), and Complex Band Ratio (e.g., Mitra et al. 2017; Abdelhady et al. 2022). MNDWI was preferred to other indices based on preliminary analysis of Landsat-5/7/8 and Sentinel-2 imagery in the study area. The results of using MNDWI and NDWI were close. So far, most studies used NDWI as an index for shoreline detection (Apostolopoulos & Nikolakopoulos 2021), and some studies demonstrated that shorelines detected using NDWI are more accurate than other methods (Apostolopoulos et al. 2020). NDWI is calculated like MNDWI with near-infrared band (NIR) instead of SWIR (McFeeters 1996). From a theoretical point of view, MNDWI is expected to work better than NDWI, especially in water regions with a background dominated by built-up land areas, because water absorbs SWIR better than NIR (Xu 2006). One of the reasons why NDVI was used more often than MNDWI is that not all satellite and aerial sensors measure SWIR. The imagery used in this study (Landsat-5/7/8 and Sentinel-2) has the SWIR band, and for this reason, we selected MNDWI as the land/water indicator.

The MNDWI calculated for “instantaneous” satellite images were averaged to composites of quarterly (3-month) periods, i.e., January–March, April–June, July–September, and October–December for each year. Selecting a 3-month temporal resolution was intended to minimize the effect of environmental errors in instantaneous images, such as wave foam, clouds, and flooded intertidal areas (García-Rubio et al. 2015; Vos et al. 2019a; Bishop-Taylor et al. 2021), and, at the same time, keep the ability to quantify intra-annual (seasonal) shoreline changes.

In parallel with calculating quarterly MNDWI time series, the MNDWI were averaged for the entire periods observed by each satellite in each region (an example in Fig. 3b). In these averaged images, “basic” SDS were detected using the sub-pixel waterline extraction algorithm (Bishop-Taylor et al. 2019). Since the threshold between water and land for MNDWI values can vary between images (Liu et al. 2012), this threshold was determined for each image using the Otsu’s thresholding algorithm, a non-parametric and unsupervised method of automatic threshold selection maximizing the separability of the resultant classes based on zeroth- and the first-order cumulative moments of the gray-level histogram (Otsu 1979).

In contrast to a traditional approach using the Digital Shoreline Analysis System (DSAS) for assessment of shoreline change along cross-shore transects (Thieler et al. 2009), in this study, we analyze the changes in the number of pixels classified as land in circular regions of 100-m radius located every 100 m along the “basic” (calculated from averaged MNDWI) SDS (total 6577 locations, an example in Fig. 3b). The size of the analyzed locations/circles ($R_c = 100$ m) was selected on the basis of the spatial resolution of the analyzed imagery (30 m). The number of pixels in each circle (about 35) was sufficient for numerical analysis, and at the same time, spatial variations in shoreline changes were not oversmoothed.

The locations of 100-m circles and the quarterly MNDWI grids were calculated from individual satellite products (Landsat-5, Landsat-7, Landsat-8, and Sentinel-2A/B) and then averaged. In each circle, the numbers of “land” pixels were calculated (all pixels whose centers were within the circle were counted) for each quarterly MNDWI composite, and then, the rate of changes of the number of “land” pixels was estimated using Sen’s non-parametric estimator of slope (Sen 1968). This robust estimator allows missing data, makes no assumptions on data distribution, and is not affected by gross data errors and outliers. As a result, all 6577 locations were classified into three classes: “land loss/erosion” (negative trend significant at 95% confidence interval), “no trend” (trend not significant), and “land gain/accretion” (positive trend significant at 95% confidence interval).

The rates of change of the numbers of “land” pixels in the 100-m circles ($\text{pixels} \cdot \text{year}^{-1}$) were transformed to linear measures of shoreline change ($\text{m} \cdot \text{year}^{-1}$) comparable to the rates obtained in the studies based on cross-shore transects. For this, the formula $E_{sh} = N_L / N_{tot} * R_c * \pi/2$ was used, where E_{sh} ($\text{m} \cdot \text{year}^{-1}$) is the linear rate of shoreline change; N_L / N_{tot} (year^{-1}) is the changes in the ratios between the number of “land” pixels to total number of pixels; and $R_c = 100$ m is the radius of the circle where the changes were measured. In other words, in each circle, the rate of shoreline change in length units (E_{sh}) was calculated as E_d / Width , where $E_d = N_L / N_{tot} * \text{Area}$ is the rate of change of the total area ($\text{Area} = \pi * R_c^2$) of “land” pixels in the circle and $\text{Width} = 2 * R_c$ is the shoreline length equal to the diameter of the circle. A similar conversion from length to area ($\text{Area} = \text{Length} * \text{Width}$) was used by Bera and Maiti (2019) when calculating land gain/loss in the Indian Sundarbans mangrove forest.

Aerial Photography

The assessments of shoreline change based on satellite imagery were compared to the data based on orthorectified aerial photography collected between 1937 and 2009 by the Shoreline Studies Program at the Virginia Institute

of Marine Science (VIMS) for the Virginia Coastal Zone Management Program at the Department of Environmental Quality (Hardaway et al. 2005; Milligan et al. 2010, 2012). Images from 1937, 1953, 1968, 1978, 1994, 2002, and 2007–2009 were utilized, and years varied in different parts of the study area. Aerial photographs were orthorectified and mosaicked to 1-m resolution images, and the shorelines were digitized in ArcMap software using USGS 30 m digital elevation model (DEM) data from the National Elevation Dataset as a vertical control.

The Digital Shoreline Analysis System (DSAS) was used to determine the rate of shoreline change (Himmelstoss et al. 2018). Baselines were created about 60 m seaward of the 1937 shoreline, and the transects perpendicular to the baseline were generated about 10 m apart. Baselines generally did not include areas that have unique shoreline morphology such as smaller creeks, creek mouths, and spits. From the intersections of the transects and shorelines, linear regression rates (LRR) were calculated by fitting a least-squares regression line to all shoreline points for given transect (see details of LRR calculation in Apostolopoulos & Nikolakopoulos 2022a). Statistical significance of each slope was assessed using a two-tailed *t*-test at 95% confidence level (Hardaway et al. 2005; Milligan et al. 2010, 2012). The rates were assigned to points at the ends of the transects. To translate their point data to our shoreline, we used GIS and a water interface shoreline created by the Center for Coastal Resources Management at VIMS. Shoreline reaches without data (typically complex areas with very low wave action) were assigned a minimal average value ($-0.03 \text{ m}\cdot\text{year}^{-1}$) from Rodriguez-Calderon (2010).

To minimize the effect of the difference in pixel size between the satellite images and aerial images, the aerial assessments were averaged within the same 100-m circles where the satellite data were processed (4530 of 6577 circles; other circles contained no aerial data). The locations where the averaged shoreline change rates were not

significantly different from zero at the 95% confidence level were classified as “no trend”, and the locations with rates significantly different from zero were classified as “land loss/erosion” and “land gain/accretion”, depending on the sign of the resulting mean. Another measure of shoreline change was qualitative categories of land loss/erosion and land gain/accretion (from “very low” to “very high”) (Table 1).

The effects of coastline morphology and man-made structures on shoreline change rates were analyzed using the Shoreline and Tidal Marsh Inventories available from the Center for Coastal Resources Management website <https://www.vims.edu/ccrm/research/inventory/index.php>. The shoreline conditions captured by these inventories include natural features like sandy beaches, detached marshes and marsh islands, artificial shore protection structures (revetments, bulkheads, marsh sills, and offshore breakwaters), and water access structures (docks, boathouses, boat ramps and marinas). Features were represented in the GIS database as lines (breakwaters, bulkheads, debris, groins, jetties, marinas, wharfs, etc.) or points (boathouses, docks, ramps, etc.) (Table 2).

Statistical Methods of Data Analysis

Temporal trends of the rates of shoreline change and regions characterized by these trends were analyzed using Empirical Orthogonal Functions (EOFs) (Preisendorfer 1988; Emery & Thomson 2014), which is a convenient method for analysis of successive images of data distributed in space. EOFs decompose time series of observations (shoreline change rates) into a set of orthogonal functions or modes. The resulting functions are uncorrelated, i.e., associated with independent natural processes. The calculations include the following operations. First, the vectors of shoreline change rates are merged into the matrix **T** with dimension $M \cdot N$, where M is the number of spatially

Table 1 The categories (grades) of shoreline evolution, including land gain (expansion, accretion) and land loss (retreat, erosion) based on the Shoreline Evolution Studies reports (Hardaway et al. 2005; Milligan et al. 2010, 2012)

Category	Land loss/gain (erosion/accretion)	[feet·year $^{-1}$] ^a	m·year $^{-1}$
+5	Very high gain (accretion)	$> +10 \text{ feet}\cdot\text{year}^{-1}$	$> +3.05 \text{ m}\cdot\text{year}^{-1}$
+4	High gain (accretion)	$+10 \text{ to } +5 \text{ feet}\cdot\text{year}^{-1}$	$+3.05 \text{ to } +1.52 \text{ m}\cdot\text{year}^{-1}$
+3	Medium gain (accretion)	$+5 \text{ to } +2 \text{ feet}\cdot\text{year}^{-1}$	$+1.52 \text{ to } +0.61 \text{ m}\cdot\text{year}^{-1}$
+2	Low gain (accretion)	$+2 \text{ to } +1 \text{ feet}\cdot\text{year}^{-1}$	$+0.61 \text{ to } +0.30 \text{ m}\cdot\text{year}^{-1}$
+1	Very low gain (accretion)	$+1 \text{ to } 0 \text{ feet}\cdot\text{year}^{-1}$	$+0.30 \text{ to } 0 \text{ m}\cdot\text{year}^{-1}$
0	No trend	No significant trend	No significant trend
-1	Very low loss (erosion)	$-1 \text{ to } 0 \text{ feet}\cdot\text{year}^{-1}$	$-0.30 \text{ to } 0 \text{ m}\cdot\text{year}^{-1}$
-2	Low loss (erosion)	$-2 \text{ to } -1 \text{ feet}\cdot\text{year}^{-1}$	$-0.61 \text{ to } -0.30 \text{ m}\cdot\text{year}^{-1}$
-3	Medium loss (erosion)	$-5 \text{ to } -2 \text{ feet}\cdot\text{year}^{-1}$	$-1.52 \text{ to } -0.61 \text{ m}\cdot\text{year}^{-1}$
-4	High loss (erosion)	$-10 \text{ to } -5 \text{ feet}\cdot\text{year}^{-1}$	$-3.05 \text{ to } -1.52 \text{ m}\cdot\text{year}^{-1}$
-5	Very high loss (erosion)	$< -10 \text{ feet}\cdot\text{year}^{-1}$	$> -3.05 \text{ m}\cdot\text{year}^{-1}$

^aThe measure used in Shoreline Evolution Studies reports (Hardaway et al. 2005; Milligan et al. 2010, 2012)

Table 2 Coastline structures stored in the Shoreline and Tidal Marsh Inventories geodatabases^a as lines and points

Coastline structures	
Lines	Points
Breakwater	Boat house
Bulkhead	Dilapidated dock
Debris	Dock
Dilapidated bulkhead	Outfall
Groin	Private ramp
Jetty	Public ramp
Marina < 50 slips	
Marina > 50 slips	
Marsh toe	
Riprap	
Unconventional	
Wharf	

^a<https://www.vims.edu/ccrm/research/inventory/index.php>

distributed points (locations where shoreline change rates were calculated), and N is the number of observations over time. Then the matrix \mathbf{T} is decomposed into two additional matrices as follows: $\mathbf{T} = \mathbf{A} \cdot \mathbf{B}$, where \mathbf{A} is $M \cdot I$ matrix and \mathbf{B} is $I \cdot N$ matrix, with I being the number of non-zero EOF modes. Each mode consists of two parts: (1) the vector of spatial distribution of a variable (loadings) and (2) a time series that quantifies how each mode changes in time (scores). The temporal resolution of the resulting time series of EOF scores is 3 months corresponding to the quarterly periods when MNDWI images were averaged. The modes are ranked according to the fraction of variance that accounted for each mode in the original data; as

a result, leading modes explain much of the variance for a given parameter. Missing data (3.28%) were reconstructed using the data interpolating empirical orthogonal functions (DINEOF) method (Beckers & Rixen 2003).

Comparison between satellite and aerial assessments of shoreline change was performed using a non-parametric method with quantitative assessments transformed to qualitative categories of land loss/erosion and land gain/accretion (from “very low” to “very high”) from the Shoreline Studies Program (<https://www.vims.edu/research/departments/physical/programs/ssp/index.php>) and converted to categories (from -5 to $+5$) in this study (Table 1), including a zero (“no trend”) category, the latter meaning the absence of a statistically significant trend at 95% confidence level. These categories are comparable to the categories (“erosion”/ “intense erosion”/ “severe erosion”) used by Luijendijk et al. (2018) studying the state of the world’s beaches and the categories used by Apostolopoulos and Nikolakopoulos (2022a; b) studying the north Peloponnese coastline.

Results

The Spatio-Temporal Patterns of Shoreline Change on the Middle Peninsula: Empirical Orthogonal Functions (EOF) Analysis

The two leading EOF modes explain 21.2% of the total variance and describe variability of shoreline change over the entire study area (Fig. 4a, b). Although the explained portion

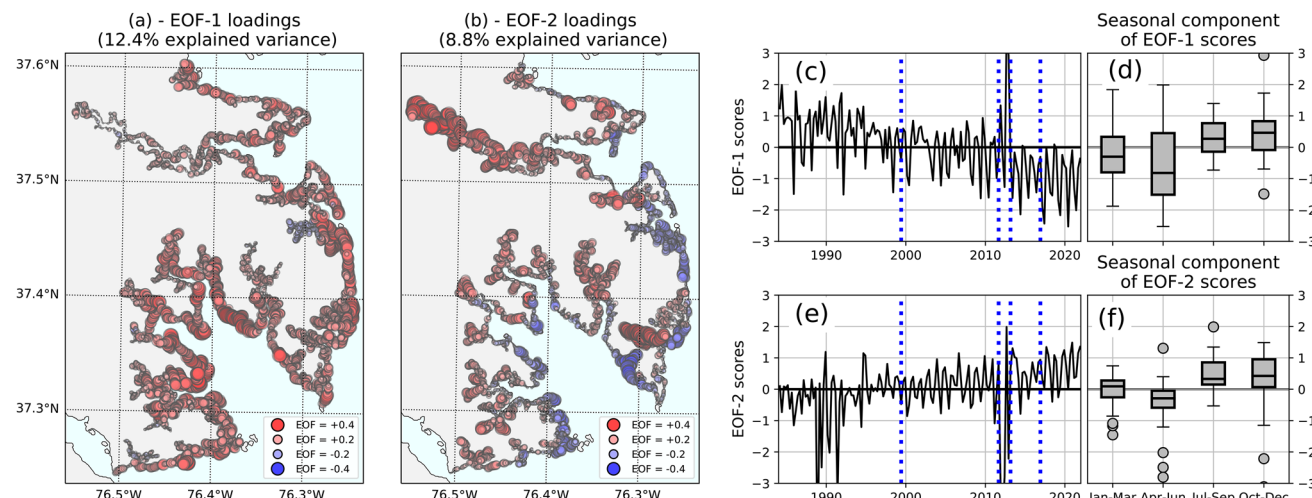


Fig. 4 The maps of EOF loadings (a, b), the time series of EOF scores (c, e), and the seasonal components of EOF scores (d, f) of the first (a, c, d) and the second (b, e, f) EOF modes of the satellite assessments of the rates of shoreline change in the Middle Peninsula of the Chesapeake Bay. The colors and sizes of EOF loadings

in a, b indicate the contribution of that location to the temporal variations of the EOF mode (c, e). Blue dotted vertical lines in time series plots (c, e) indicate the dates when the number of observing satellites changed, from one satellite (Landsat-5) to four satellites (Landsat-7/8 and Sentinel-2A/B) (see Fig. 2)

of total variance is comparatively small, we focus on these two modes because the modes of lower rank represent variations in restricted parts of the Middle Peninsula and demonstrate no evident trends and patterns.

The scores (time series) of both leading EOF modes include outliers between the Fall of 2011 and the Spring of 2013 (Fig. 4c, e), when satellite data were collected by Landsat-7 satellite only. The low quality of satellite imagery during this period is not surprising taking into account well-known problems of Landsat-7 ETM + Scan Line Corrector (SLC)-off gap striping (Maxwell et al. 2007; Lee et al. 2016; Li et al. 2017).

The first EOF mode explains 12.4% of the total variance and demonstrates that the entire Middle Peninsula is affected by intensive land loss processes (Fig. 4a). Most of the observed locations demonstrate the same sign of variations, highest loadings along exposed reaches of shoreline, evident linear decreasing trend (land loss/erosion) (Fig. 4c), and insignificant seasonal variations (Fig. 4d). This mode is associated with continual erosion over the entire Middle Peninsula.

The second EOF mode (explains 8.8% of total variance) can be attributed to the accuracy of shoreline detection in inlets and embayments, which may be affected by seasonal cycles of alongshore vegetation. The EOF-2 loadings are most pronounced in the inlets, including an estuary of

the Piankatank River in the northern part of the study area (Fig. 4b). EOF-2 scores demonstrate no significant trend (Fig. 4e) and seasonal variations (Fig. 4f) with negative rates of shoreline change (land loss) in spring and positive rates (land gain) in summer-fall. We attribute these variations to a seasonal cycle of vegetation (designated by MNDWI as land) along the shoreline. Different types of vegetation reflect green and infrared radiance (from which MNDWI is calculated) in different ways and their seasonal changes can affect the balance between green and infrared and, as a result, have an effect on the SDS location associated with the zone of maximum MNDWI gradient. In other words, vegetation affects SDS, the shoreline detected from satellite imagery, rather than the physical edge between land and water.

This assumption is supported by loose but significant correlations between EOF-2 loadings and certain types of alongshore land cover associated with different types of vegetation. The second EOF mode loadings were positively correlated with the portions of shoreline classified as agricultural, residential, and grass land cover types (Fig. 5a). Also, the EOF-2 loadings were negatively correlated with the areas classified as marshes and scrub/shrub (Fig. 5b). We speculate that all these land cover types are associated with vegetation whose seasonal variability affected MNDWI and SDS in different ways.

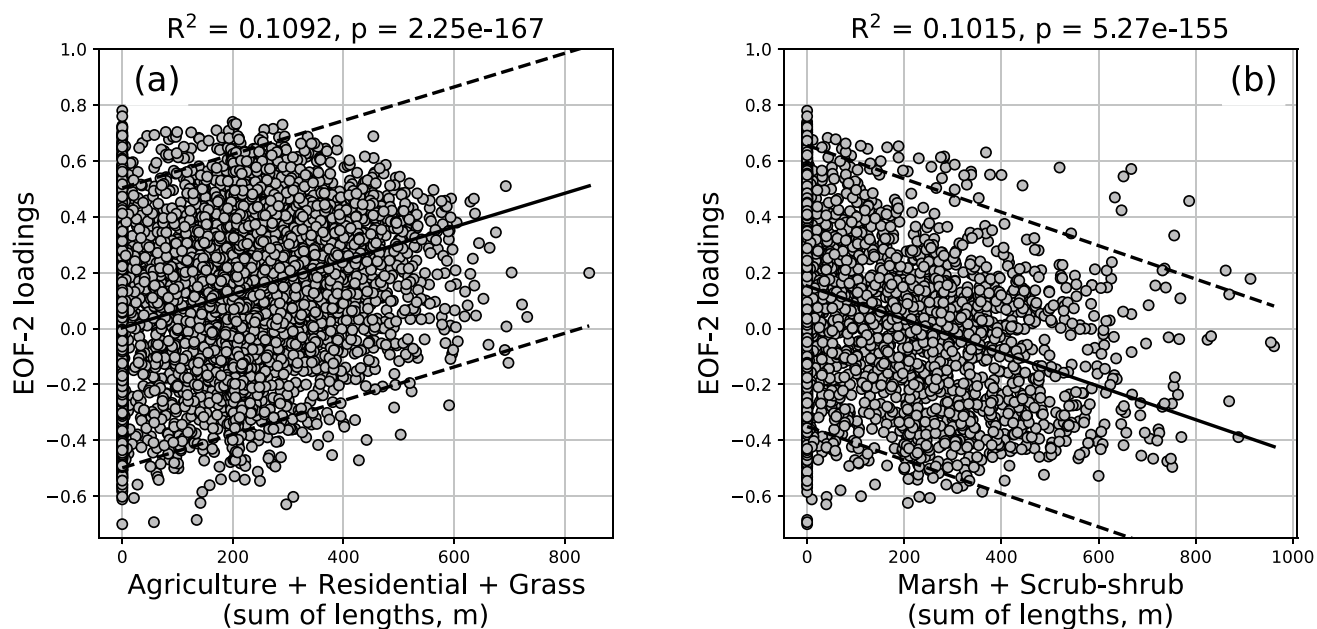


Fig. 5 Correlations between the loadings of the second EOF mode and the shoreline land cover types. X-axes in **a** and **b** include the sum of the lengths of “agriculture”, “residential”, and “grass” (**a**) and the sum of the lengths of “marsh” and “scrub-shrub” (**b**) within the

100-m circles where land gain/loss was assessed. Sums of the lengths are used instead of percentage because the shoreline land cover types in the shoreline and tidal marsh inventories geodatabase can overlap

Disagreement Between the Satellite and Aerial Assessments of Shoreline Change

The disagreement between satellite imagery and aerial photography assessments can be evaluated in different ways. Considering only the directions of shoreline change (“land loss/erosion”, “no trend”, or “land gain/accretion”), we find that the agreement is not high, which can be attributed to (1) different periods of assessment, 1937–2009 for aerial photography vs. 1984–2021 for satellite imagery, and (2) the differences between detection of the land/water edge from the two data sources. Only 46.4% of the studied locations demonstrate agreement (Table 3). Most of the disagreement, however, resulted from the very high number (53%) of locations where “no trend” was found in satellite data. Absolute disagreement (“land loss/erosion” in one data source and “land gain/accretion” in another) was observed in only 5.6% of the analyzed locations. Total Spearman’s rank correlation between the two types of measurements was low but significant ($\rho=0.173$; $p<10^{-31}$).

Including more grades into the shoreline change assessments (from “very low” to “very high”, following the approach used by the Shoreline Studies Program (Milligan et al. 2010, 2012) (Table 1)), considerably improved the correlation between the two assessments ($\rho=0.331$; $p<10^{-115}$) (Table 4).

The maps of the grades of shoreline change obtained by both methods were similar, with maximum changes (mostly “land loss/erosion”) occurring along exposed reaches of shoreline (Fig. 6a, b). For example, in locations where erosion rates exceeded 3 m year⁻¹, the total shoreline retreat during the 38 years of satellite imagery was greater than 100 m. Few locations, however, demonstrated evident disagreement (Fig. 6c, d) probably resulting from the differences in the periods of assessment. Detailed analysis of the VIMS reports (Hardaway et al. 2005; Milligan et al. 2010, 2012) revealed that in many locations the periods of “land loss/erosion” were followed by the periods of “no trend” or “land gain/accretion” and vice versa. As a result, the rates of shoreline change based on aerial photography (1937–2009) differed from the assessments based on satellite imagery collected considerably later (1984–2021) (Fig. 2).

Table 3 Correspondence between the numbers of alongshore locations (100-m circles) attributed to categories “land loss/erosion”, “no trend”, and “land gain/accretion”

Aerial photography (1937–2009)	Satellite imagery (1984–2021)			
	Land loss/erosion	No trend	Land gain/accretion	Total
Land loss/erosion	1596 (35%)	1724 (38%)	169 (3.7%)	3489 (77%)
No trend	191 (4.2%)	495 (11%)	58 (1.3%)	744 (16%)
Land gain/accretion	81 (1.8%)	178 (3.9%)	38 (0.8%)	297 (6.6%)
Total	1868 (41%)	2397 (53%)	265 (5.8%)	4530 (100%)

The total number of locations in the table (4530) is lower than the total number of locations with satellite data (6577) because some locations (circles) contained no aerial assessments

The Effect of Coastal Morphology, Land Cover, and Man-made Structures on Shoreline Change

The shoreline segments most subject to change were sandy beaches, i.e., the locations (100-m circles) where the total length of “beach” segments obtained from the shoreline and tidal marsh inventories geodatabase exceeded 90% of the total shoreline length. Among these locations, the percentage of sites with medium to high “land loss/erosion” and “land gain/accretion” exceeded the mean values for the entire study region by a factor of 4 (erosion 32.1–34.7% at beaches vs. 8.0–10.6% total; accretion 4.1–4.5% at beaches vs. 0.9–0.8% total; Fig. 7b; Table 5). In the study area, the chance of beaches to experience erosion (32.1–34.7%) exceeded the world’s average (24%) reported by Luijendijk et al. (2018). At the same time, the chance of accretion (4.1–4.5%) was much lower compared to 28% reported by Luijendijk et al. (2018). These figures were similar for both satellite and aerial assessments (Table 5).

Very different rates of shoreline change were found in the locations with a significant amount of marshes (wetlands). In locations (100-m circles) where the total length of “detached marshes” and “marsh islands” exceeded 50 m, satellite data demonstrated a high (> 30%) percentage subject to medium to high “land loss/erosion”; this figure, however, was not confirmed by aerial data (10.3%; Fig. 7c; Table 5), which was close to the total average (8.0%; Fig. 7a; Table 5). We speculate that this difference results from the fact that in wetlands/marshes aerial surveys and satellite imagery detect shoreline differently. In wetlands, high-resolution aerial photography reveals the boundary between land and water even when water is covered by vegetation. In contrast, satellite pixels over wetlands are classified as “land” because their optical signatures are dominated by light reflected by vegetation rather than water. As a result, satellite assessments demonstrated that shorelines in “marsh” areas were retreating during 1984–2021 at higher rates compared with aerial assessments. Also, the number of “marsh” locations subject to accretion was zero in both satellite and aerial data.

The presence of man-made structures demonstrated a stabilizing effect on the shoreline (Fig. 7d, e; Table 5).

Table 4 The numbers of alongshore locations (100-m circles) classified as different categories of “land loss/erosion” (from “very high” to “very low”), “no trend”, and “land gain/accretion” (from “very low” to “very high”) (for categories, see Table 1)

Aerial photography (1937–2009)	Satellite imagery (1984–2021)					No trend	Land gain/accretion	+1	+2	+3	+4	+5	Total
	-5	-4	-3	-2	-1								
Land loss/erosion	-5	2	0	1	0	2	1	0	0	0	0	0	6
-4	11	40	12	2	3	13	0	1	2	1	0	0	85
-3	6	16	87	47	31	67	8	3	3	2	0	0	270
-2	0	5	143	192	90	217	8	8	1	0	0	0	664
-1	0	7	108	369	424	1425	93	29	8	1	0	0	2464
No trend	0	1	1	20	62	107	495	40	13	4	1	0	744
Land gain/accretion	+1	0	2	3	17	26	145	18	2	2	1	0	216
+2	0	0	3	1	7	21	2	1	3	0	0	0	38
+3	0	2	9	2	2	9	1	1	1	4	1	32	8
+4	0	0	0	0	2	2	3	1	0	0	0	0	3
+5	0	0	1	2	0	0	0	0	0	0	0	0	1
Total	20	73	387	696	692	2397	172	58	24	10	1	1	4530

The presence of hardened structures (such as bulkheads, revetments, and offshore breakwaters) resulted in a decrease of both erosion and accretion rates. This decrease, however, was more pronounced in satellite assessments compared to aerial measurements; we attribute this difference to the fact that many man-made structures were created after the 1960s–1970s and affected satellite assessments more than aerial surveys.

Discussion

This study demonstrates the effectiveness of using Landsat and Sentinel-2 imagery for the routine assessment of tidal shoreline changes, including both straight and complex shorelines. The range of shoreline change rates detected from satellite data on the Middle Peninsula, Virginia (lower Chesapeake Bay), was comparable to the rates detected from conventional aerial photography analysis. Using imagery from multiple satellites over a period of almost four decades allowed for detailed evaluation of shoreline dynamics at high spatial and temporal scales, which supports the idea that using multiple sensors can improve temporal resolution of shoreline detection, remove short-term variability, and reduce uncertainties in satellite-derived shoreline analysis compared to a low-frequency sampling approach (Adebisi et al. 2021).

In this study, the changes in the numbers of “land” vs. “water” pixels were analyzed in circular regions of fixed (100 m) radius, rather than the traditional method of cross-shore transects (Thieler et al. 2009; Vos et al. 2019b). The process of generating transects orthogonal to the coast is straightforward only for shorelines with relatively simple morphologies, such as beaches, and can be performed without manual corrections of software-generated results. However, for coastlines with complex morphologies such as those around river deltas and salt marshes, where the waterline is more fragmented and difficult to identify (Shaw et al. 2008), the transect-based indicator often fails to characterize the coastline position and its change over time (Xu 2018). As a result, most studies analyzing shoreline change focus on shorelines with simple morphologies such as beaches (Luijendijk et al. 2018) and skip the locations where a transect-based approach does not work (Luijendijk et al. 2018; Armstrong & Lazarus 2019; Vos et al. 2020). In contrast, the method used in this study works well for both straight and complex shorelines and does not require laborious and expensive manual work, making it applicable in any coastal region. The approach used in this study has some common features with the shoreline movement algorithm used by Abdelhady et al. (2022), which also did not use cross-shore transects and was based on categorizing the pixels in the target shoreline according to distance from the reference shoreline.

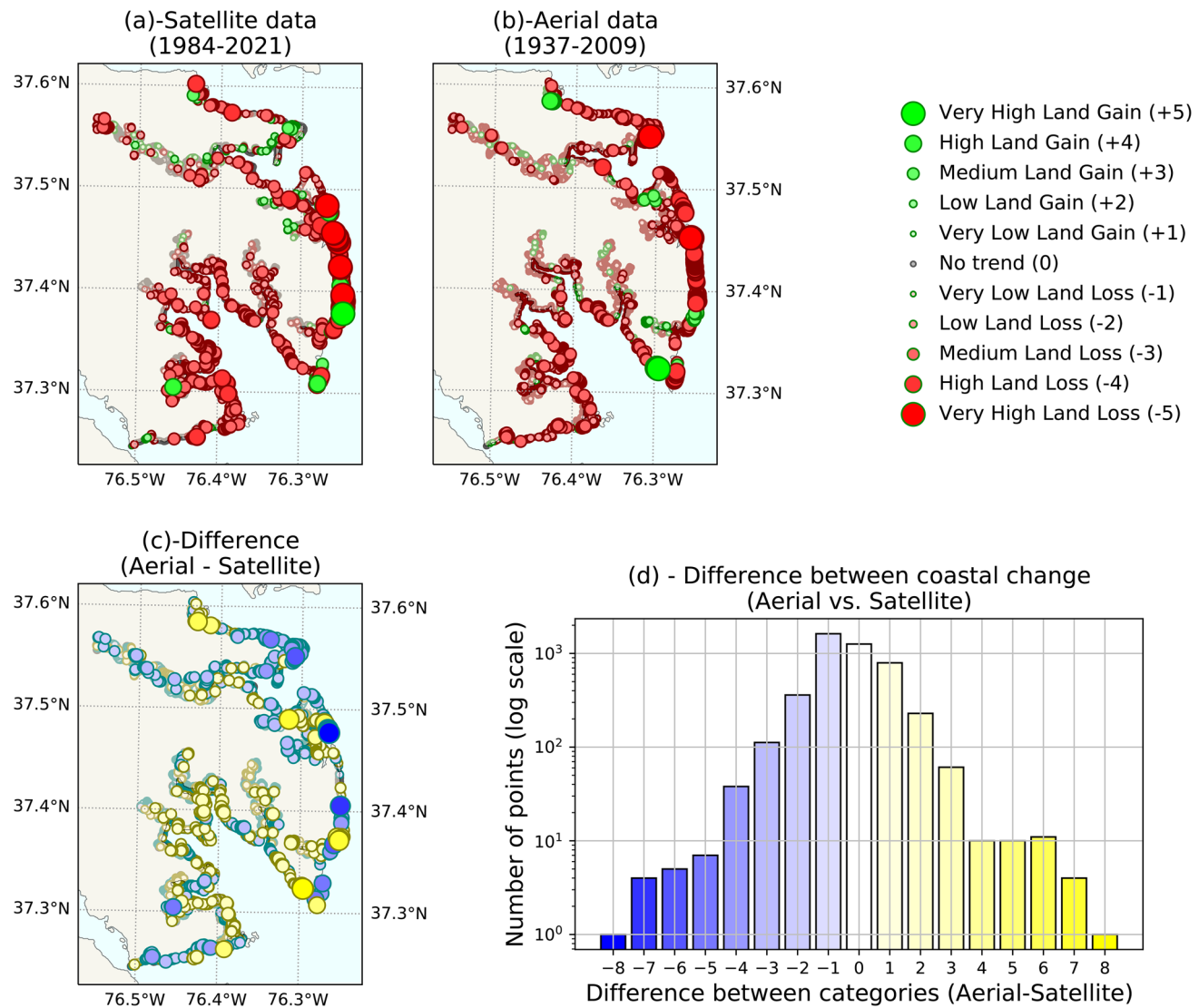


Fig. 6 Assessments of shoreline change from satellite (a) and aerial (b) data using the categories of “land gain”/“land loss” (Table 1). The map (c) and the histogram (d) demonstrate the differences between the assessments (aerial minus satellite)

The limitations of using satellite data to detect shoreline changes result from inaccurate detection of the land–water boundary. One reason is associated with bright targets such as sand or whitewater in the surf zone which can be misclassified as clouds (Zhu & Woodcock 2012). Highly turbid water also makes an accurate extraction of the land/water boundary difficult (Teodoro & Goncalves 2012; Chen et al. 2019). Large vessels next to the shoreline can also result in SDS displacement (Chen et al. 2019; Apostolopoulos et al. 2020). Bright targets cause other issues; e.g., the boundary between whitewater and normal water can be easily confused with shoreline (Hagenaars et al. 2018; Pardo-Pascual et al. 2018).

Variation of alongshore vegetation can also be misinterpreted as satellite-derived shoreline (SDS) expansion/

retreat (Pardo-Pascual et al. 2012). In temperate latitudes, the changes in vegetation canopy follow seasonal patterns, and we speculate that it was radiance reflected by vegetation that produced seasonal variations of the second EOF mode rather than the movements of shoreline itself. This hypothesis agrees with the results of Pardo-Pascual et al. (2012), who compared the period when the area they studied on the Spanish Mediterranean coast was occupied by natural vegetation and the period when this vegetation disappeared, and found large (up to 45 m) differences in the location of SDS. These variations cannot be attributed to sediment transport, although previous studies documented seasonal cycles in this process (Castelle et al. 2021), with sediments eroded from the foreshore during initial winter storms and migrating back shoreward (to the beach face)

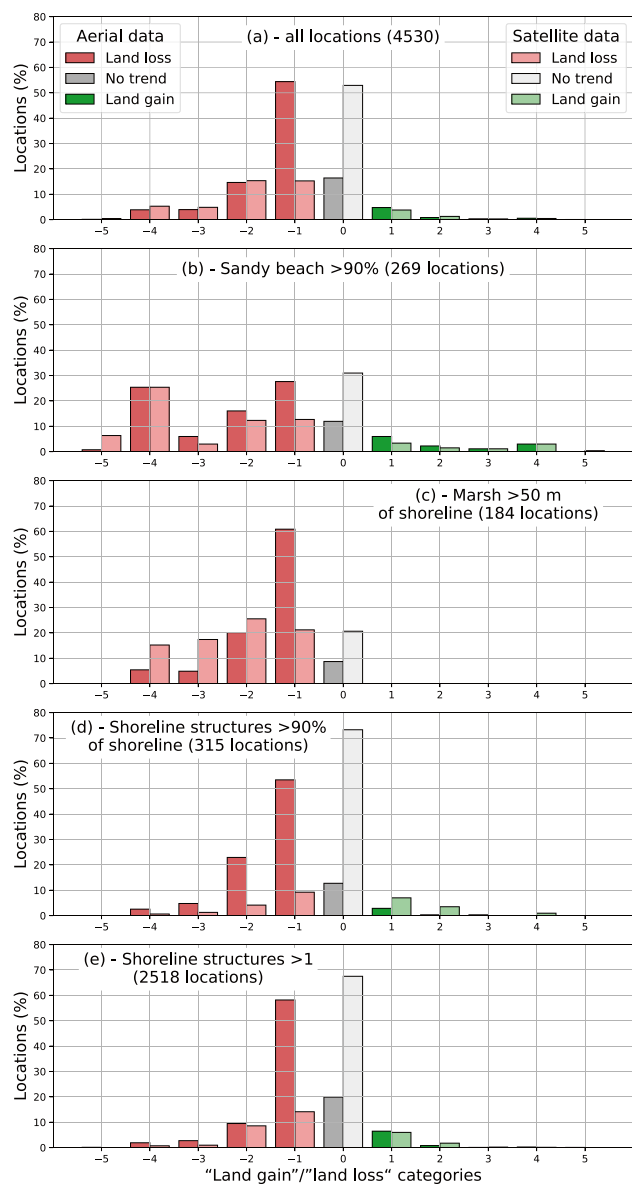


Fig. 7 Histograms of shoreline change rates detected from satellite and aerial data under different shoreline conditions. **a** All locations (100-m circles); **b** sandy beaches; **c** marshes; **d** shoreline structures stored in geodatabase as lines (Table 2); **e** shoreline structures stored in geodatabase as points (Table 2). X-axes in **a–e** indicate the categories of “land gain”/“land loss” (Table 1). See footnotes in Table 5 for explanation how beaches, marshes, and structures were detected in 100-m circles

during less energetic summer periods (Aubrey 1979). Also, some beaches change grain size (e.g., from sand to gravel) between the seasons, influencing the visibility of the shoreline indicator and shifting the shoreline proxy (McAllister et al. 2022). These effects, however, are typical to open shoreline reaches affected by winds, waves, tides, and currents. In contrast, according to the results of this study, a seasonal cycle was most evident in inlets and embayments

where the effect of waves and currents was expected to be small. We conclude that these variations resulted from a seasonal cycle of vegetation obscuring accurate detection of the shoreline.

An additional source of incorrect detection of shoreline change is expected in the areas with barrier islands separating open ocean from back-barrier waters (bays, lagoons, and tidal creek systems) (see FitzGerald et al. 2008). When these barriers are treated as shorelines, the “water” pixels in the circles of 100-m radius include both open waters, back-barrier waters, and tidal inlets. Land retreat associated with RSLR in such areas often starts with an increase of the areas covered by back-barrier waters with coastline remaining at the same position or even migrating offshore (FitzGerald et al. 2008; Passeri et al. 2015), resulting in disagreement between land loss assessed by our method and by the method based on cross-shore transects.

In wetlands (marshes), high rates of shoreline retreat observed from satellite data indicate intensive transformation of marshes to open water environment (marsh drowning) resulting from RSLR, which accelerated from 1.6–1.8 mm year⁻¹ over the twentieth century (Church & White 2006, 2011; Jevrejeva et al. 2006, 2008) to 3.3 ± 0.3 mm year⁻¹ over 1993–2019 (The Climate Change Initiative Coastal Sea Level Team 2020). The period observed by aerial photography was earlier (Fig. 2), and the percentage of “marsh” locations with shoreline retreat was much lower (Table 5). It should be noted that the process of marsh drowning is non-linear, highly complex, and site-specific (Passeri et al. 2015) and depends on factors such as sediment supply, vegetation productivity, rates of subsidence or uplift, changes in storm frequency and intensity, and availability of inland areas for migration (Stralberg et al. 2011). At low rates of RSLR, marsh vegetation remains within the same location due to vertical accretion, i.e., accumulation of sediments on the marsh platform (Mariotti & Fagherazzi 2010; Stralberg et al. 2011; Townend et al. 2011). At higher rates of RSLR, conversion of marsh to open water usually occurs in the interior of the marsh, not at the marsh edge, and the marsh drowns only after RSLR exceeds the rate of accretion (Reed 1990).

In recent decades, the acceleration of RSLR has led to an increase in shoreline retreat (Church & White 2006, 2011; Cazenave & Llovel 2010). This study demonstrated that in locations with man-made structures, this process was slower as compared to natural parts of the coast. Previous studies showed that human modification of coastlines has had a varying impact on shoreline change. On the one hand, some developed areas have experienced reduced erosion owing to cumulative sediment input (e.g., areas of beach nourishment, which adds sand to beach from outside sources) (Armstrong & Lazarus 2019) and creation and maintenance of coastal infrastructure (Hapke et al. 2013; Mendoza et al. 2022). On the other hand, shoreline structures such as offshore

Table 5 The percentage of locations (100-m circles) with medium/high shoreline change rates (categories –3 to –5 and +3 to +5; see Table 1) depending on the shoreline features (sandy beaches), land cover (marshes) and man-made structures

Shoreline morphology/land cover/man-made structures	Medium/high land loss (erosion)		Medium/high land gain (accretion)	
	Aerial photography	Satellite imagery	Aerial photography	Satellite imagery
Beaches (> 90% of shoreline) ^a	32.1%	34.7%	4.1%	4.5%
Marsh (≥ 50 m) ^b	10.3%	32.6%	0.0%	0.0%
“Line” structures (> 90% of shoreline) ^c	7.3%	1.9%	0.3%	1.0%
“Point” structures (all)	4.8%	1.7%	0.4%	0.3%
“Point” structures (boathouses)	2.9%	0.3%	0.5%	0.2%
“Point” structures (docks)	5.0%	1.7%	0.4%	0.3%
“Point” structures (ramps)	6.5%	0.6%	0.0%	0.6%
“Point” structures (outfalls)	0.0%	9.1%	0.0%	0.0%
Total shoreline	8.0%	10.6%	0.9%	0.8%

^aThe “beach” percentage of shoreline was calculated as the length of “beach” line feature within the 100-m circle divided by the sum of “beach” and “not beach” line features within the same 100-m circle

^bWe use the total length of “marsh” features within the 100-m circles instead of percentage of shoreline because “marsh” group includes “detached marshes” and “marsh islands”, which are not parts of shoreline

^cThe percentages of “line” man-made structures (Table 2) were calculated as the sums of the lengths of these line features within the 100-m circle divided by the sum of all line features within the same 100-m circle

breakwaters can disrupt the natural longshore transport of sand and cause or worsen erosion on nearby properties (Saengsupavanich et al. 2022). However, in our study area the stabilizing effect of artificial structures was more pronounced than their negative effect on coastal erosion.

The approach used in this study is not free of flaws resulting mostly from inaccurate detection of the edge between land and water. This issue, however, can be improved using advanced approaches of shoreline detection. Recent studies introduced different deep learning or machine learning approaches, resulting in higher accuracy and greater sensitivity to fine-scale, narrow coastline features (Erdem et al. 2021; McAllister et al. 2022; Pucino et al. 2022; Seale et al. 2022). Additional improvement of shoreline detection can be achieved by classifying image pixels into more than two classes (land and water), including sand, whitewater (Vos et al. 2019a, b), rip currents, breaking zone, and beach face (Teodoro et al. 2011). Further improvement of the assessment technology combining greater data availability provided by a data cube technology and unified methods of accurate shoreline detection is a promising approach supplying valuable information for coastal risk management.

Conclusions

The results of this study highlight the effectiveness of using Landsat and Sentinel-2 imagery in quantitatively assessing shoreline dynamics. The approach, which was based on the variations of the land/water ratio within small alongshore regions, provides reliable assessments even for shorelines

with complex morphology where conventional methods based on cross-shore transects are not feasible. The use of cloud-based data cube technologies significantly enhances the processing capabilities of large amounts of satellite information. The comparison of shoreline change demonstrates reasonable agreement with traditional aerial assessments, considering differences in the analyzed time periods and the accuracy of land–water edge detection.

Acknowledgements This work was supported in part by the US Bipartisan Infrastructure Law (BIL), as well as the National Oceanic and Atmospheric Administration/National Environmental Satellite, Data, and Information Service (NOAA/NESDIS) Ocean Remote Sensing (ORS) Program. Part of this work was performed and funded under ST13301CQ0050/1332KP22FNEED0042. This work was carried out on the Committee on Earth Observation Satellites (CEOS) Earth Analytics Interoperability Laboratory (EAIL) system which was developed with the support of Commonwealth Scientific and Industrial Research Organization (CSIRO) and with funding from National Aeronautics and Space Administration (NASA). We thank Prasanjit Dash (Cooperative Institute for Research in the Atmosphere, Colorado State University) for including the numerical results of this study into the Application Knowledge Hub (AKH; <https://www.star.nesdis.noaa.gov/socd/coast/>). The comments of two anonymous reviewers were thoughtful and greatly improved the final manuscript. The scientific results and conclusions, as well as any views or opinions expressed herein, are those of the authors and do not necessarily reflect those of NOAA or the Department of Commerce.

Author Contribution NPN: investigation, data processing and analysis, writing—original draft. JDH: investigation, formal analysis, writing—review and editing. JH: development of the method, writing—review and editing. SS: conceptualization, development of the method, writing—review and editing. RBT: conceptualization, development of the method. GZ: conceptualization, writing—review and editing. PDG: conceptualization, funding acquisition, project administration, supervision.

Data Availability The shoreline and tidal marsh inventories are available from the Center for Coastal Resources Management website <https://www.vims.edu/ccrm/research/inventory/index.php>. The Python codes of the data analysis are available by request from the corresponding author. The resulting assessments of shoreline change are available from the Application Knowledge Hub (AKH) website <https://www.star.nesdis.noaa.gov/socd/coast/> (open access planned since May 2023).

Declarations

Conflict of Interest The authors declare no competing interests.

References

- Abdelhady, H. U., C.D. Troy, A. Habib, and R. Manish. 2022. A simple, fully automated shoreline detection algorithm for high-resolution multi-spectral imagery. *Remote Sensing* 14 (3): 557. <https://doi.org/10.3390/rs14030557>.
- Adebisi, N., A.-L., Balogun, M., Mahdianpari, and T. H. Min. 2021. Assessing the impacts of rising sea level on coastal morphodynamics with automated high-frequency shoreline mapping using multi-sensor optical satellites. *Remote sensing* 13(18): 3587. <https://doi.org/10.3390/rs13183587>.
- Almonacid-Caballer, J., E. Sánchez-García, J.E. Pardo-Pascual, A.A. Balaguer-Beser, and J. Palomar-Vázquez. 2016. Evaluation of annual mean shoreline position deduced from Landsat imagery as a mid-term coastal evolution indicator. *Marine Geology* 372: 79–88. <https://doi.org/10.1016/j.margeo.2015.12.015>.
- Apostolopoulos, D., and K. Nikolakopoulos. 2021. A review and meta-analysis of remote sensing data, GIS methods, materials and indices used for monitoring the coastline evolution over the last twenty years. *European Journal of Remote Sensing* 54 (1): 240–265. <https://doi.org/10.1080/22797254.2021.1904293>.
- Apostolopoulos, D., and K. Nikolakopoulos. 2022a. Identifying sandy sites under erosion regime along the Prefecture of Achaia, using remote sensing techniques. *Journal of Applied Remote Sensing* 17 (2): 022206. <https://doi.org/10.1117/1.JRS.17.022206>.
- Apostolopoulos, D., K. Nikolakopoulos, V. Boumpoulis, and N. Depouintis. 2020. GIS-based analysis and accuracy assessment of low-resolution satellite imagery for coastline monitoring. *SPIE Proceedings 11534, Earth Resources and Environmental Remote Sensing/GIS Applications XI: 115340B*. <https://doi.org/10.1117/12.2573440>.
- Apostolopoulos, D. N., and K.G. Nikolakopoulos. 2022b. SPOT vs Landsat satellite images for the evolution of the north Peloponnesus coastline, Greece. *Regional Studies in Marine Science* 56: 102691. <https://doi.org/10.1016/j.rsma.2022.102691>.
- Armstrong, S.B., and E.D. Lazarus. 2019. Masked shoreline erosion at large spatial scales as a collective effect of beach nourishment. *Earth's Future* 7 (2): 74–84. <https://doi.org/10.1029/2018EF001070>.
- Aschbacher, J., and M.P. Milagro-Pérez. 2012. The European Earth Monitoring (GMES) Programme: Status and perspectives. *Remote Sensing of Environment* 120: 3–8. <https://doi.org/10.1016/j.rse.2011.08.028>.
- Aubrey, D.G. 1979. Seasonal patterns of onshore/offshore sediment movement. *Journal of Geophysical Research: Oceans* 84 (C10): 6347–6354. <https://doi.org/10.1029/JC084iC10p06347>.
- Beckers, J.-M., and M. Rixen. 2003. EOF calculations and data filling from incomplete oceanographic datasets. *Journal of Atmospheric and Oceanic Technology* 20 (12): 1839–1856. [https://doi.org/10.1175/1520-0426\(2003\)020%3c1839:ECADFF%3e2.0.CO;2](https://doi.org/10.1175/1520-0426(2003)020%3c1839:ECADFF%3e2.0.CO;2).
- Bera, R., and R. Maiti. 2019. Quantitative analysis of erosion and accretion (1975–2017) using DSAS — a study on Indian Sundarbans. *Regional Studies in Marine Science* 28: 100583. <https://doi.org/10.1016/j.rsma.2019.100583>.
- Bishop-Taylor, R., R. Nanson, S. Sagar, and L. Lymburner. 2021. Mapping Australia's dynamic coastline at mean sea level using three decades of Landsat imagery. *Remote Sensing of Environment* 267: 112734. <https://doi.org/10.1016/j.rse.2021.112734>.
- Bishop-Taylor, R., S. Sagar, L. Lymburner, I. Alam, and J. Sixsmith. 2019. Sub-pixel waterline extraction: Characterising accuracy and sensitivity to indices and spectra. *Remote Sensing* 11 (24): 2984. <https://doi.org/10.3390/rs11242984>.
- Boak, E.H., and I.L. Turner. 2005. Shoreline definition and detection: A review. *Journal of Coastal Research* (214): 688–703. <https://doi.org/10.2112/03-0071.1>.
- Castelle, B., G. Masselink, T. Scott, C. Stokes, A. Konstantinou, V. Marieu, and S. Bujan. 2021. Satellite-derived shoreline detection at a high-energy meso-macrotidal beach. *Geomorphology* 383: 107707. <https://doi.org/10.1016/j.geomorph.2021.107707>.
- Cazenave, A., and W. Llovel. 2010. Contemporary sea level rise. *Annual Review of Marine Science* 2 (1): 145–173. <https://doi.org/10.1146/annurev-marine-120308-081105>.
- Chen, C., J. Fu, S. Zhang, and X. Zhao. 2019. Coastline information extraction based on the tasseled cap transformation of Landsat-8 OLI images. *Estuarine, Coastal and Shelf Science* 217: 281–291. <https://doi.org/10.1016/j.ecss.2018.10.021>.
- Church, J.A., and N.J. White. 2006. A 20th century acceleration in global sea-level rise. *Geophysical Research Letters* 33 (1). <https://doi.org/10.1029/2005GL024826>.
- Church, J.A., and N.J. White. 2011. Sea-level rise from the late 19th to the early 21st century. *Surveys in Geophysics* 32 (4): 585–602. <https://doi.org/10.1007/s10712-011-9119-1>.
- Drusch, M., U. Del Bello, S. Carlier, O. Colin, V. Fernandez, F. Gascon, and P. Bargellini. 2012. Sentinel-2: ESA's optical high-resolution mission for GMES operational services. *Remote Sensing of Environment* 120: 25–36. <https://doi.org/10.1016/j.rse.2011.11.026>.
- Emery, W.J., and R.E. Thomson. 2014. *Data analysis methods in physical oceanography*. Amsterdam: Elsevier Science.
- Erdem, F., B. Bayram, T. Bakirman, O.C. Bayrak, and B. Akpinar. 2021. An ensemble deep learning based shoreline segmentation approach (WaterNet) from Landsat 8 OLI images. *Advances in Space Research* 67 (3): 964–974. <https://doi.org/10.1016/j.asr.2020.10.043>.
- FitzGerald, D.M., M.S. Fenster, B.A. Argow, and I.V. Buynevich. 2008. Coastal impacts due to sea-level rise. *Annual Review of Earth and Planetary Sciences* 36 (1): 601–647. <https://doi.org/10.1146/annurev.earth.35.031306.140139>.
- García-Rubio, G., D. Huntley, and P. Russell. 2015. Evaluating shoreline identification using optical satellite images. *Marine Geology* 359: 96–105. <https://doi.org/10.1016/j.margeo.2014.11.002>.
- Giuliani, G., J. Masó, P. Mazzetti, S. Nativi, and A. Zabala. 2019. Paving the way to increased interoperability of Earth observations data cubes. *Data* 4 (3): 113. <https://doi.org/10.3390/data4030113>.
- Hagenaars, G., S. de Vries, A.P. Luijendijk, W.P. de Boer, and A.J.H.M. Reniers. 2018. On the accuracy of automated shoreline detection derived from satellite imagery: A case study of the sand motor mega-scale nourishment. *Coastal Engineering* 133: 113–125. <https://doi.org/10.1016/j.coastaleng.2017.12.011>.
- Hapke, C.J., M.G. Kratzmann, and E.A. Himmelstoss. 2013. Geomorphic and human influence on large-scale coastal change. *Geomorphology* 199: 160–170. <https://doi.org/10.1016/j.geomorph.2012.11.025>.

- Hardaway, C.S., Jr., D.A. Milligan, L.M. Varnell, C.A. Wilcox, and G.R. Thomas. 2005. *Shoreline evolution Chesapeake Bay and Piankatank River shorelines Mathews County, VA*. Retrieved from <https://scholarworks.wm.edu/reports/265/>.
- Hardaway, C.S., Jr., and R.J. Byrne. 1999. *Shoreline management in Chesapeake Bay. Special Report in Applied Marine Science and Ocean Engineering* (356). Retrieved from <https://scholarworks.wm.edu/reports/581/>.
- Himmelstoss, E.A., R.E. Henderson, M.G. Kratzmann, and A.S. Farris. 2018. *Digital Shoreline Analysis System (DSAS) version 5.0 user guide* (2018–1179). Retrieved from <http://pubs.er.usgs.gov/publication/ofr20181179>.
- Jevrejeva, S., A. Grinsted, J.C. Moore, and S. Holgate. 2006. Nonlinear trends and multiyear cycles in sea level records. *Journal of Geophysical Research: Oceans* 111 (C9): C09012. <https://doi.org/10.1029/2005JC003229>.
- Jevrejeva, S., J.C. Moore, A. Grinsted, and P.L. Woodworth. 2008. Recent global sea level acceleration started over 200 years ago? *Geophysical Research Letters* 35 (8): L08715. <https://doi.org/10.1029/2008GL033611>.
- Lee, S., M. Cho, and C.-W. Lee. 2016. An effective gap filtering method for Landsat ETM+ SLC-off data. *Terrestrial Atmospheric and Oceanic Sciences* 27 (6): 921–932. <https://doi.org/10.3319/TAO.2016.07.18.02>.
- Lewis, A., S. Oliver, L. Lymburner, B. Evans, L. Wyborn, N. Mueller, and L.-W. Wang. 2017. The Australian Geoscience Data Cube — foundations and lessons learned. *Remote Sensing of Environment* 202: 276–292. <https://doi.org/10.1016/j.rse.2017.03.015>.
- Li, C., Y. Zheng, and Y. Wu. 2017. Recovering missing pixels for Landsat ETM + SLC-off imagery using HJ-1A /1B as auxiliary data. *International Journal of Remote Sensing* 38 (11): 3430–3444. <https://doi.org/10.1080/01431161.2017.1295484>.
- Liu, Y., P. Song, J. Peng, and C. Ye. 2012. A physical explanation of the variation in threshold for delineating terrestrial water surfaces from multi-temporal images: Effects of radiometric correction. *International Journal of Remote Sensing* 33 (18): 5862–5875. <https://doi.org/10.1080/01431161.2012.675452>.
- Loveland, T.R., and J.L. Dwyer. 2012. Landsat: Building a strong future. *Remote Sensing of Environment* 122: 22–29. <https://doi.org/10.1016/j.rse.2011.09.022>.
- Luijendijk, A., G. Hagenaars, R. Ranasinghe, F. Baart, G. Donchyts, and S. Aarninkhof. 2018. The state of the world's beaches. *Scientific Reports* 8 (1): 6641. <https://doi.org/10.1038/s41598-018-24630-6>.
- Lyard, F.H., D.J. Allain, M. Cancet, L. Carrère, and N. Picot. 2021. FES2014 global ocean tide atlas: Design and performance. *Ocean Science* 17 (3): 615–649. <https://doi.org/10.5194/os-17-615-2021>.
- Mariotti, G., and S. Fagherazzi. 2010. A numerical model for the coupled long-term evolution of salt marshes and tidal flats. *Journal of Geophysical Research: Earth Surface* 115 (F1). <https://doi.org/10.1029/2009JF001326>.
- Maxwell, S.K., G.L. Schmidt, and J.C. Storey. 2007. A multi-scale segmentation approach to filling gaps in Landsat ETM+ SLC-off images. *International Journal of Remote Sensing* 28 (23): 5339–5356. <https://doi.org/10.1080/01431160601034902>.
- McAllister, E., A. Payo, A. Novellino, T. Dolphin, and E. Medina-Lopez. 2022. Multispectral satellite imagery and machine learning for the extraction of shoreline indicators. *Coastal Engineering* 174: 104102. <https://doi.org/10.1016/j.coastaleng.2022.104102>.
- McFeeters, S.K. 1996. The use of the Normalized Difference Water Index (NDWI) in the delineation of open water features. *International Journal of Remote Sensing* 17 (7): 1425–1432. <https://doi.org/10.1080/01431169608948714>.
- Mendoza, E.T., A. Torres-Freyermuth, E. Ojeda, G. Medellín, R. Rioja-Nieto, P. Salles, and I. Turki. 2022. Seasonal changes in beach resilience along an urbanized barrier island. *Frontiers in Marine Science* 9: 889820. <https://doi.org/10.3389/fmars.2022.889820>.
- Mentaschi, L., M.I. Vousdoukas, J.-F. Pekel, E. Voukouvalas, and L. Feyen. 2018. Global long-term observations of coastal erosion and accretion. *Scientific Reports* 8 (1): 12876. <https://doi.org/10.1038/s41598-018-30904-w>.
- Milligan, D.A., C. Wilcox, C.S. Hardaway, and M.C. Cox, Jr. 2012. *Shoreline evolution: Middlesex County, Virginia Rappahannock River and Piankatank River shorelines*. Retrieved from <https://scholarworks.wm.edu/reports/370/>.
- Milligan, D.A., K.P. O'Brien, C. Wilcox, and C.S. Hardaway, Jr. 2010. *Shoreline evolution: Gloucester County, Virginia York River, Mobjack Bay, and Piankatank River shorelines*. Retrieved from <https://scholarworks.wm.edu/reports/567/>.
- Mills, A.K., P. Ruggiero, J.P. Bolte, K.A. Serafin, and E. Lipiec. 2021. Quantifying uncertainty in exposure to coastal hazards associated with both climate change and adaptation strategies: A U.S. Pacific Northwest alternative coastal futures analysis. *Water* 13 (4): 545. <https://doi.org/10.3390/w13040545>.
- Mitra, S.S., D. Mitra, and A. Santra. 2017. Performance testing of selected automated coastline detection techniques applied on multispectral satellite imagers. *Earth Science Informatics* 10 (3): 321–330. <https://doi.org/10.1007/s12145-017-0289-3>.
- Murray, N.J., S.P. Phinn, R.A. Fuller, M. DeWitt, R. Ferrari, R. Johnston, and M.B. Lyons. 2022. High-resolution global maps of tidal flat ecosystems from 1984 to 2019. *Scientific Data* 9 (1): 542. <https://doi.org/10.1038/s41597-022-01635-5>.
- Nanson, R., R. Bishop-Taylor, S. Sagar, and L. Lymburner. 2022. Geomorphic insights into Australia's coastal change using a national dataset derived from the multi-decadal Landsat archive. *Estuarine, Coastal and Shelf Science* 265: 107712. <https://doi.org/10.1016/j.ecss.2021.107712>.
- Neumann, B., A.T. Vafeidis, J. Zimmermann, and R.J. Nicholls. 2015. Future coastal population growth and exposure to sea-level rise and coastal flooding - a global assessment. *PLoS One* 10 (3): e0118571. <https://doi.org/10.1371/journal.pone.0118571>.
- O'Hara, C.C., and B.S. Halpern. 2022. Anticipating the future of the world's ocean. *Annual Review of Environment and Resources* 47 (1): 291–315. <https://doi.org/10.1146/annurev-environ-120120-053645>.
- Otsu, N. 1979. A threshold selection method from gray level histograms. *IEEE Transactions on Systems, Man, and Cybernetics* 9: 62–66. <https://doi.org/10.1109/TSMC.1979.4310076>.
- Pardo-Pascual, J.E., J. Almonacid-Caballer, L.A. Ruiz, and J. Palomar-Vázquez. 2012. Automatic extraction of shorelines from Landsat TM and ETM+ multi-temporal images with subpixel precision. *Remote Sensing of Environment* 123: 1–11. <https://doi.org/10.1016/j.rse.2012.02.024>.
- Pardo-Pascual, J.E., E. Sánchez-García, J. Almonacid-Caballer, J.M. Palomar-Vázquez, E. Priego de los Santos, A. Fernández-Sarría, and A. Balaguer-Beser. 2018. Assessing the accuracy of automatically extracted shorelines on microtidal beaches from Landsat 7, Landsat 8 and Sentinel-2 imagery. *Remote Sensing* 10 (2): 326. <https://doi.org/10.3390/rs10020326>.
- Parthasarathy, K.S.S., and P.C. Deka. 2021. Remote sensing and GIS application in assessment of coastal vulnerability and shoreline changes: A review. *ISH Journal of Hydraulic Engineering* 27 (sup1): 588–600. <https://doi.org/10.1080/09715010.2019.1603086>.
- Passeri, D.L., S.C. Hagen, S.C. Medeiros, M.V. Bilskie, K. Alizad, and D. Wang. 2015. The dynamic effects of sea level rise on low-gradient coastal landscapes: A review. *Earth's Future* 3 (6): 159–181. <https://doi.org/10.1002/2015EF000298>.
- Pekel, J.-F., A. Cottam, N. Gorelick, and A.S. Belward. 2016. High-resolution mapping of global surface water and its long-term changes. *Nature* 540 (7633): 418–422. <https://doi.org/10.1038/nature20584>.
- Pope, J.P., and T.J. Burbey. 2004. Multiple-aquifer characterization from single borehole extensometer records. *Groundwater* 42 (1): 45–58. <https://doi.org/10.1111/j.1745-6584.2004.tb02449.x>.

- Preisendorfer, R.W. 1988. *Principal Component Analysis in meteorology and oceanography*. New York, NY: Elsevier Science.
- Pucino, N., D.M. Kennedy, M. Young, and D. Ierodiaconou. 2022. Assessing the accuracy of Sentinel-2 instantaneous subpixel shorelines using synchronous UAV ground truth surveys. *Remote Sensing of Environment* 282: 113293. <https://doi.org/10.1016/j.rse.2022.113293>.
- Rahman, M. K., T.W. Crawford, and M.S. Islam. (2022). Shoreline change analysis along rivers and deltas: A systematic review and bibliometric analysis of the shoreline study literature from 2000 to 2021. *Geosciences*, 12(11): 410. <https://doi.org/10.3390/geosciences12110410>.
- Reed, D.J. 1990. The impact of sea-level rise on coastal salt marshes. *Progress in Physical Geography: Earth and Environment* 14 (4): 465–481. <https://doi.org/10.1177/030913339001400403>.
- Rodriguez-Calderon, C. 2010. *Spatial and temporal patterns in erosional and depositional processes: Physical and biological controls in the York River, Chesapeake Bay, Virginia*. (Master of Science Dissertations, Theses, and Masters Projects), College of William and Mary, ProQuest LLC. Retrieved from <https://scholarworks.wm.edu/etd/1539617897/>.
- Saengsupavanich, C., E. H. Ariffin, L.S. Yun, and D.A. Pereira. 2022. Environmental impact of submerged and emerged breakwaters. *Heliyon* 8 (12): e12626. <https://doi.org/10.1016/j.heliyon.2022.e12626>.
- Seale, C., T. Redfern, P. Chatfield, C. Luo, and K. Dempsey. 2022. Coastline detection in satellite imagery: A deep learning approach on new benchmark data. *Remote Sensing of Environment* 278: 113044. <https://doi.org/10.1016/j.rse.2022.113044>.
- Sen, P.K. 1968. Estimates of the regression coefficient based on Kendall's tau. *Journal of the American Statistical Association* 63 (324): 1379–1389. <https://doi.org/10.1080/01621459.1968.10480934>.
- Shaw, J.B., M.A. Wolinsky, C. Paola, and V.R. Voller. 2008. An image-based method for shoreline mapping on complex coasts. *Geophysical Research Letters* 35 (12): L12405. <https://doi.org/10.1029/2008GL033963>.
- Small, C., and R. Nicholls. 2003. A global analysis of human settlement in coastal zones. *Journal of Coastal Research* 19 (3): 584–599. <https://doi.org/10.2307/4299200>.
- Splinter, K.D., M.D. Harley, and I.L. Turner. 2018. Remote sensing is changing our view of the coast: Insights from 40 years of monitoring at Narrabeen-Collaroy, Australia. *Remote Sensing* 10 (11): 1744. <https://doi.org/10.3390/rs10111744>.
- Stralberg, D., M. Brennan, J.C. Callaway, J.K. Wood, L.M. Schile, D. Jongsomjit, and S. Crooks. 2011. Evaluating tidal marsh sustainability in the face of sea-level rise: A hybrid modeling approach applied to San Francisco Bay. *PLoS One* 6 (11): e27388. <https://doi.org/10.1371/journal.pone.0027388>.
- Sudmanns, M., H. Augustin, B. Killough, G. Giuliani, D. Tiede, A. Leith, and A. Lewis. 2022. Think global, cube local: An Earth Observation Data Cube's contribution to the Digital Earth vision. *Big Earth Data*. <https://doi.org/10.1080/20964471.2022.2099236>.
- Teodoro, A.C., and H. Gonçalves. 2012. A semi-automatic approach for the extraction of sandy bodies (sand spits) from IKONOS-2 data. *IEEE Journal of Selected Topics in Applied Earth Observations and Remote Sensing* 5 (2): 634–642. <https://doi.org/10.1109/JSTARS.2011.2181339>.
- Teodoro, A., J. Pais-Barbosa, H. Gonçalves, F. Veloso-Gomes, and F. Taveira-Pinto. 2011. Identification of beach hydromorphological patterns/forms through image classification techniques applied to remotely sensed data. *International Journal of Remote Sensing* 32 (22): 7399–7422. <https://doi.org/10.1080/01431161.2010.523729>.
- The Climate Change Initiative Coastal Sea Level Team. 2020. Coastal sea level anomalies and associated trends from Jason satellite altimetry over 2002–2018. *Scientific Data* 7 (1): 357. <https://doi.org/10.1038/s41597-020-00694-w>.
- Thieler, E.R., and W.W. Danforth. 1994. Historical shoreline mapping (I): Improving techniques and reducing positioning errors. *Journal of Coastal Research* 10 (3): 549–563.
- Thieler, E.R., E.A. Himmelstoss, J.L. Zichichi, and A. Ergul. 2009. *The Digital Shoreline Analysis System (DSAS) Version 4.0 - an ArcGIS extension for calculating shoreline change*. Retrieved from <http://pubs.er.usgs.gov/publication/ofr20081278>.
- Townend, I., C. Fletcher, M. Knappen, and K. Rossington. 2011. A review of salt marsh dynamics. *Water and Environment Journal* 25 (4): 477–488. <https://doi.org/10.1111/j.1747-6593.2010.00243.x>.
- Verpoorter, C., T. Kutser, D.A. Seekell, and L.J. Tranvik. 2014. A global inventory of lakes based on high-resolution satellite imagery. *Geophysical Research Letters* 41 (18): 6396–6402. <https://doi.org/10.1002/2014GL060641>.
- Vos, K., M.D. Harley, K.D. Splinter, J.A. Simmons, and I.L. Turner. 2019a. Sub-annual to multi-decadal shoreline variability from publicly available satellite imagery. *Coastal Engineering* 150: 160–174. <https://doi.org/10.1016/j.coastaleng.2019.04.004>.
- Vos, K., M.D. Harley, K.D. Splinter, A. Walker, and I.L. Turner. 2020. Beach slopes from satellite-derived shorelines. *Geophysical Research Letters* 47(14): e2020GL088365. <https://doi.org/10.1029/2020GL088365>.
- Vos, K., K.D. Splinter, M.D. Harley, J.A. Simmons, and I.L. Turner. 2019b. CoastSat: a Google Earth Engine-enabled Python toolkit to extract shorelines from publicly available satellite imagery. *Environmental Modelling & Software* 122: 104528. <https://doi.org/10.1016/j.envsoft.2019.104528>.
- Xiao, X., S. Boles, S. Frolik, W. Salas, B. Moore, C. Li, and R. Zhao. 2002. Observation of flooding and rice transplanting of paddy rice fields at the site to landscape scales in China using VEGETATION sensor data. *International Journal of Remote Sensing* 23(15): 3009–3022. <https://doi.org/10.1080/01431160110107734>.
- Xu, H. 2006. Modification of Normalised Difference Water Index (NDWI) to enhance open water features in remotely sensed imagery. *International Journal of Remote Sensing* 27 (14): 3025–3033. <https://doi.org/10.1080/01431160600589179>.
- Xu, N. 2018. Detecting coastline change with all available Landsat data over 1986–2015: A case study for the state of Texas, USA. *Atmosphere* 9 (3): 107. <https://doi.org/10.3390/atmos903107>.
- Zhong, L., and M. Li. 2006. Tidal energy fluxes and dissipation in the Chesapeake Bay. *Continental Shelf Research* 26 (6): 752–770. <https://doi.org/10.1016/j.csr.2006.02.006>.
- Zhong, L., M. Li, and M.G.G. Foreman. 2008. Resonance and sea level variability in Chesapeake Bay. *Continental Shelf Research* 28 (18): 2565–2573. <https://doi.org/10.1016/j.csr.2008.07.007>.
- Zhu, Z., and C.E. Woodcock. 2012. Object-based cloud and cloud shadow detection in Landsat imagery. *Remote Sensing of Environment* 118: 83–94. <https://doi.org/10.1016/j.rse.2011.10.028>.

Springer Nature or its licensor (e.g. a society or other partner) holds exclusive rights to this article under a publishing agreement with the author(s) or other rightsholder(s); author self-archiving of the accepted manuscript version of this article is solely governed by the terms of such publishing agreement and applicable law.